The Evolution of Springtime Water Vapor Over Beijing Observed by a High Dynamic Raman Lidar System: Case Studies

Tianning Su, Jian Li, Jing Li, Chengcai Li, Yiqi Chu, Yiming Zhao, Jianping Guo, Yong Yu, and Lidong Wang

***Abstract*—Raman lidar is an effective technique to retrieve the vertical distribution of atmospheric water vapor. For the first time, we present water vapor profiles retrieved by a high dynamic Raman lidar system over the Beijing area for representative cases in spring 2014, within the framework of the Aerosol Multi-wavelength Polarization Lidar Experiment project. In springtime, water vapor content over Beijing is generally low but with a strong daily variability. Its evolution is strongly coupled with winds and aerosols, with clouds also exerting a distinct impact. Northwesterly winds is found to be the most important factor impacting the temporal variability of water vapor mixing ratio (WVMR), and WVMR is found to be negatively correlated with wind speed. Moreover, we find that clouds tend to cause significant increases in the standard deviation of WMVR measurement, and relative humidity sharply increase below the cloud base. During a typical pollution episode, water vapor strongly covaries with aerosols due to hygroscopic growth effect and transport mechanism. Both water vapor and aerosols exhibit the highest variability within the planetary boundary layer (PBL), where the development and dissipation of haze mainly occur. Within the PBL, water vapor and aerosol concentration demonstrate different evolution features at different altitudes during the haze process, with a delayed increase and early decrease for higher altitudes. Back trajectory analysis using the hybrid single-particle Lagrangian trajectory model indicates that this phenomenon is most likely associated with different sources of the air mass at different altitudes.**

***Index Terms*—Aerosols, atmospheric measurements, clouds, humidity, wind.**

I. Introduction

DESPITE its low content in the atmosphere, water vapor is a very active element and a primary greenhouse gas [1]. Water vapor exerts significant impacts on precipitation, global energy balance and climate variability of the earth-atmosphere system [2]. These important influences of water vapor are closely related to its vertical distribution and temporal variation [3]. However, it is difficult to obtain precise distribution of water vapor due to its rapid evolution [4], especially in some atmospheric processes (e.g., cloud formation and gale). Therefore, detailed examination of water vapor variability during these atmospheric processes is particularly important.

The climate in Beijing represents typical meteorological conditions of the North China Plain. In summer, the weather in Beijing is dominated by East Asian monsoon with moisture transported from the seaward, and is hot and humid, while in winter it is strongly affected by the vast Siberian anticyclones, and is cold and dry. In spring, however, the weather in Beijing is complex, and the water vapor content is relatively low but is characterized by rapid change and large variability associated with varying wind conditions. To track this highly variable water vapor content in spring and examine the detailed environmental condition, high temporal and spatial resolution measurements of water vapor are required. Moreover, as Beijing has been increasingly experiencing severe haze pollution in spring in recent years [5], [6], and as water vapor is closely related to the haze formation, it is necessary to simultaneously examine the evolution of water vapor and aerosol cycles in order to study their coupling effect. However, till now, the evolution features of water vapor in Beijing are still not well understood, partly due to the lack of high-resolution water vapor observations.

Various methods have been developed to measure the water vapor, including radiosonde (RS), satellite, microwave radiometer, solar radiometer, and Raman lidar. RS is among one of the most accurate means to measure water vapor, but lacks the capability of continuous sampling [7]. Satellite with a sensor unit can obtain water vapor information on global scale, but is limited by accuracy and vertical information [8]. Ground-based microwave radiometer and solar radiometer can provide water vapor measurement with high temporal resolution, but the

Manuscript received July 15, 2016; revised November 24, 2016; accepted January 6, 2017. Date of publication March 15, 2017; date of current version April 10, 2017. This work was supported in part by the National Natural Science Foundation of China under Grant 41375008 and Grant 41175020, in part by the "Strategic Priority Research Program" of the Chinese Academy of Sciences under Grant XDA05040203, in part by the President's Undergraduate Research Fellowship of Peking University, and in part by the National High Technology Research and Development Program of China through the 863 Major Project under Grant SQ2010AA1221583001. *(Corresponding author: Chengcai Li.)*

T. Su is with the Department of Atmospheric and Oceanic Sciences, Peking University, Beijing 100871, China, and also with the Department of Atmospheric and Oceanic Sciences, University of Maryland, College Park, MD 20740 USA (e-mail: tianningsu1994@gmail.com).

J. Li, J. Li, C. Li, and Y. Chu are with the Department of Atmospheric and Oceanic Sciences, Peking University, Beijing 100871, China (e-mail: lijian08@pku.edu.cn; jing-li@pku.edu.cn; ccli@pku.edu.cn; chuyiqi@pku.edu.cn).

Y. Zhao, Y. Yu, and L. Wang are with Beijing Research Institute of Telemetry, Beijing 100076, China (e-mail: zym_bird@126.com; yuy_1971@126.com; wanglidong021@163.com).

J. Guo is with the State Key Laboratory of Severe Weather, Chinese Academy of Meteorological Sciences, Beijing 100081, China (e-mail: jpguo@camscma.cn).

Color versions of one or more of the figures in this paper are available online at http://ieeexplore.ieee.org.

Digital Object Identifier 10.1109/JSTARS.2017.2653811

vertical resolution is coarse and bears a high uncertainty [9]. As an active remote sensing instrument, Raman lidar has the capability of both accurately measuring water vapor and achieving relatively high vertical and temporal resolutions, and has thus been extensively applied to detect the distribution and variation of atmospheric water vapor [10]–[12].

With the development of lidar technique, state of the art Raman lidar systems show excellent capabilities in water vapor observation, and have been extensively used for water vapor retrieval over worldwide locations. For example, using this technique, Wang *et al.* [13] presented long-term water vapor measurements retrieved over Hefei characterized with its seasonality. Froidevaux *et al*. [14] measured water vapor in the planetary boundary layer (PBL) with particularly high vertical and temporal resolutions. Dionisi *et al.* [15] retrieved water vapor profiles up to the lower stratosphere with high precision. Foth *et al.* [16] presented a method to derive water vapor profiles from Raman lidar automatically calibrated by the integrated water vapor. Wu *et al*. [17] reported the water vapor fluxes over the Tibetan Plateau based on the Raman lidar measurements. However, there is still lack of high-resolution water vapor measurements in North China Plain, which hinders the investigation of major factors impacting water vapor variability over this megacity area. In particular, the mechanism causing the rapid change of water vapor content during springtime remains poorly understood.

Among the factors influencing water vapor content, clouds and winds play particularly important roles. On one hand, clouds can disturb Raman signal, due to the fact that the intensity of Raman scattering is much weaker than Mie-Rayleigh scattering and thus attenuates rapidly in cloud layers. This mechanism prevents precise detection of water vapor above clouds. On the other hand, water vapor and aerosols are both involved in the cloud formation, as cloud droplet formation is related to the condensation of water vapor on ambient aerosols [18]. Clouds also are known to contain masses of liquid droplets and nearly saturated water vapor, and have significant impact on water vapor content of the surrounding atmosphere. In addition, convection and radiation are also critical influential factors in determining the distribution of water vapor in the daytime [19]. At night, the effect of radiation is negligible, whereas winds have a major impact on the transport of water vapor and aerosols.

As part of the Aerosol Multi-wavelength Polarization Lidar Experiment (AMPLE) project, a new, versatile and portable Raman scanning lidar system has been designed and developed in Beijing [20]. With high pulses repetition rate (1000 Hz) and output power ($\sim$1 W), the AMPLE lidar system is able to detect the dynamic variation of water vapor and aerosols with high temporal and vertical resolutions, which allows for insightful studies on the detailed atmospheric and weather processes. Complementary to the technical parameters of AMPLE in [20], we here present the performance of AMPLE in detection of water vapor mixing ratio (WVMR) and aerosol extinction coefficients (AEC) in detail over Beijing, and investigate the variability of water vapor associated with clouds, wind and pollution, in order to clarify the mechanisms responsible for the water vapor variability. In Section II, we make a brief introduction of the AMPLE system and the observation site. The methods for obtaining WVMR and calibration constant are described in Section III. Section IV presents the retrieved water vapor profile and its coupling with clouds, winds, and aerosols. A brief summary of this paper is given in Section V.

TABLE I
TECHNICAL PARAMETERS OF THE AMPLE RAMAN LIDAR

Laser source	
Laser	Diode pumped Nd:YAG
Output wavelength	532 and 355 nm
Output power	0.6 W at 355 nm; 1.5 W at 532 nm;
Pulse repetition rate	1000 Hz
Pulse width	$\sim$1 ns
Linear polarization	$>$100:1
Receiver system	
Elastic channels	355 and 532 nm
Raman channels	386 nm (N_2) and 407 nm (H_2O)
Depolarization	355 and 532 nm
Telescope	
Type	20 cm Cassegrain
Field of view	1 mrad
Scanning system	
Scanning speed	20°/smax
Scanning angle error	$<$0.2°

II. MEASUREMENT FACILITIES

A. AMPLE System

AMPLE measures Raman backscattered signals at 386 and 407 nm wavelengths, which are used to retrieve WVMR profile. Meanwhile, the elastic backscatter signals at 355 and 532 nm are simultaneously measured by the same lidar. The repetition rate of the laser source is relatively high, which enhances the signal dynamic range. Due to the contamination by sunlight, Raman backscatter signal cannot be effectively detected during the daytime; thus, the data of Raman backscatter signal is only obtained at night in our experiment. Specifically, AMPLE receives Raman backscatter signals from 22:00 to 05:00 each night. The vertical resolution of the raw data is 19.8 m, and the original 2-s data have been further averaged over 60-s intervals to improve signal-to-noise ratio (SNR). All measurements are taken in the vertical orientation. Background subtraction, saturation, afterpulse, overlap and range corrections are applied to raw lidar data to derive the range-squared-corrected signal (RSCS). The main technical parameters of the Raman Lidar system AMPLE are presented in I.

B. Observation Sites

The AMPLE system was installed at Peking University (39°59.5'N, 116°18.6'E, elevation 50 m), which is located in the northwest of the Beijing metropolitan area. Due to the limitation of our experiment, there is lack of collocated RS measurements with the lidar data. We therefore employ atmospheric profile data obtained from the RS station (39°48'N, 116°28.2'E,

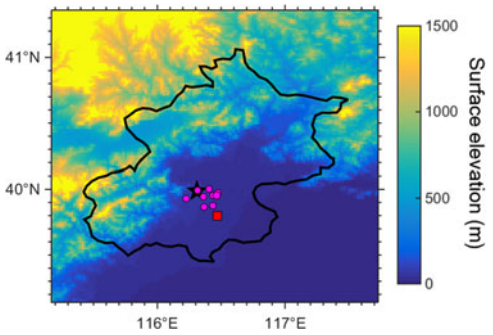

Fig. 1. Topography condition of Beijing. The black curve represents the provincial boundary of Beijing. The black star indicates the lidar site. The red square represents the location of the RS station. The pink dots indicate the nine environmental monitoring stations within 20 km from lidar site.

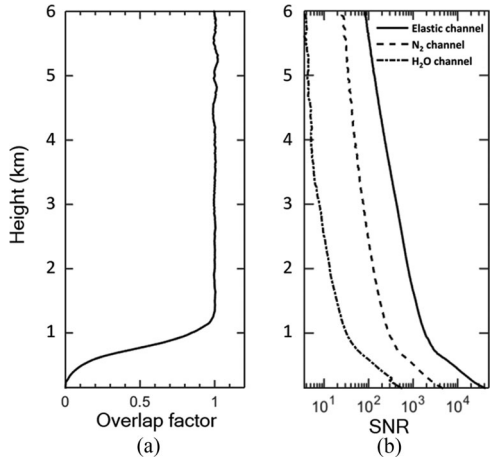

Fig. 2. (a) AMPLE'S overlap factors for the 355 nm elastic channels. (b) SNR profiles for three channels (elastic, N_2-Raman and H_2O-Raman) derived from a lidar profile with time interval of 60 min (an average over 3 600 000 laser shots) on 00:00 CST May 2, 2014.

elevation 30 m, ~25 km from Peking university) of Beijing operated by China Meteorological Administration. The used variables include the profiles of water vapor, temperature, pressure and wind, provided by RS which is launched around 07:15 Chinese Standard Time (CST) and 19:15 CST for each day. The original RS data are detected per second, and the vertical resolution of RS profile is altitude dependent and less than 8 m in our cases [44]. For comparing with lidar profile, the RS profile has been averaged to achieve a vertical resolution of 30 m. The surface wind speed (WS) and wind direction (WD) in 30-min interval are obtained from the automatic wind measuring system near the lidar system.

To reduce small scale bias and obtain a stable regional variation of particulate matter with the diameter smaller than 2.5 μm ($PM_{2.5}$) and those with the diameter smaller than 10 μm (PM_{10}), we acquire mean $PM_{2.5}$ and PM_{10} data from nine environmental monitoring stations within 20 km from the lidar site, including one station of Beijing Embassy of United States and eight stations of Chinese Ministry of Environmental Protection. These data can serve as a representative of air pollution conditions around lidar site.

The topography of Beijing is presented in Fig. 1. The black star indicates the lidar site, the red square represents the location of the RS station, and the pink dots indicate the nine environmental monitoring stations within 20 km from lidar site. All of the meteorological and environmental stations are within 26 km centered at lidar site, and share the similar geographic condition with lidar site. Therefore, we consider that the meteorological and environmental conditions at these observation sites can well represent those of the lidar site.

III. Methodology

A. Retrieval Process and Error Estimation

In this study, we use previously well-established algorithm to retrieve WVMR. Detailed description of the method can be found in [21]–[23]. The relationship between WVMR and the Raman signals is described by the following equation:

$$w(z) = C_w \frac{P_{\mathrm{H_2O}}(z)}{P_{\mathrm{N_2}}(z)} \Delta q \tag{1}$$

where $\Delta q = \exp[-\int_0^z (\alpha^m_{\mathrm{N_2}} + \alpha^p_{\mathrm{N_2}})dr] / \exp[-\int_0^z (\alpha^m_{\mathrm{H_2O}} + \alpha^p_{\mathrm{H_2O}})dr]$, C_w is the Raman lidar calibration constant, which is calculated by the corresponding RS data. $P_{\mathrm{H_2O}}$ and $P_{\mathrm{N_2}}(z)$ are the Raman backscatter signal at the wavelength of 407 and 386 nm, respectively. Δq represents the differential transmission ratio between 386 and 407 nm, which can be simultaneously estimated by the additional channels of the AMPLE lidar. $\alpha^m_{\mathrm{H_2O}}$ and $\alpha^m_{\mathrm{N_2}}$ are molecular extinction coefficients at 407 and 386 nm, respectively. This part can be calculated by the temperature and pressure profiles from RS at the same day [24]. $\alpha^p_{\mathrm{H_2O}}$ and $\alpha^p_{\mathrm{N_2}}$ are AEC at 407 and 386 nm, respectively, which can be calculated by the Klett method [25]. Here, we use the Klett method to retrieve AEC. The Klett solutions are integrated by starting from a far and clear range, which is selected as 7 km above ground level in this study. Linear relationship between extinction and backscatter coefficients is usually prescribed in the retrieval process, and a 50 sr of the column-averaged extinction-to-backscatter ratio (the so-called lidar ratio) is used here, which is a typical value in the troposphere [26]. The retrieval processes for AEC are strongly influenced by the overlap effect. Note that in (1) identical overlap factors are generally assumed, which means that the overlap factors for H_2O and N_2 channel are equivalent. The overlap factor for elastic channels can be experimentally determined [27]. Fig. 2(a) presents the overlap factor for 355 nm elastic channel; the overlap factor approximates to 1 above 1200 m.

The performance of the system has been analyzed in terms of SNR, namely the ratio between the lidar signal and the lidar statistical error. Assuming the distribution of Poisson statistics, SNR at channel of wavelength λ can be given as follows [28]:

$$\mathrm{SNR}_\lambda = \frac{S_\lambda + B_\lambda}{\sqrt{S_\lambda + {\sigma_{BH}}^2}} \tag{2}$$

where S_λ represents the lidar raw signal at wavelength λ, and B_λ is background signal, which is computed by averaging the signal return from above 30 km. ${\sigma_{BH}}^2$ are the background noise. For a

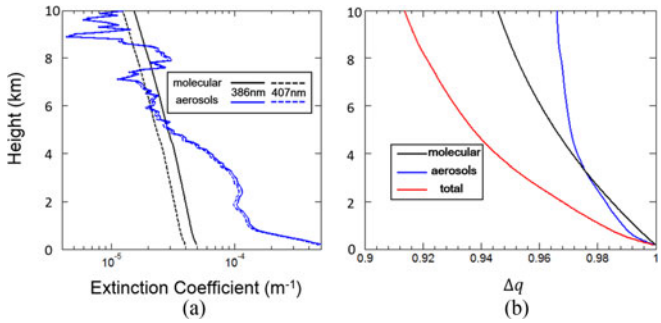

Fig. 3. (a) Profiles of molecular and AEC at 386 and 407 nm. (b) Differential transmission ratio Δq including the molecular (black) and aerosols (blue) contribution and the total (red).

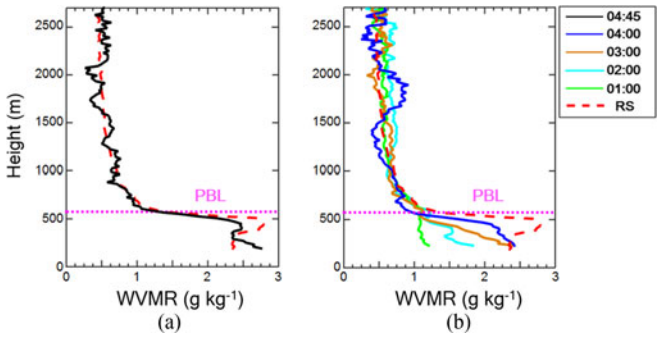

Fig. 4. WVMR measured by AMPLE and RS. The black, blue, brown, light blue, and green curves indicate the profile of WVMR at 04:45, 04:00, 03:00, 02:00 and 01:00 CST on March 2, 2014, respectively. The RS was launched at 07:15 CST on March 2. The pink-dashed line represents the PBL determine by AMPLE at 07:00 CST on March 2.

larger number of laser shots p, the SNR can be easily calculated knowing that it is proportional to $\sqrt{p}$. In Fig. 2(b), SNR of three channels is given for a lidar signal acquired on 00:00 CST May 2, 2014 with time interval of 60 min (an average over 3 600 000 laser shots). The relative error of the WMVR measurement can be written as follows:

$$\frac{\Delta w}{w} = \sqrt{\left(\frac{1}{\mathrm{SNR}_1}\right)^2 + \left(\frac{1}{\mathrm{SNR}_2}\right)^2} \tag{3}$$

where SNR_1 and SNR_2 represent the SNR at the H_2O and N_2 channels, respectively. Δw characterizes the statistical error of the WV measurement. As $\mathrm{SNR}_2 \gg \mathrm{SNR}_1$, the relative error approximates to $1/\mathrm{SNR}_1$. In this case, the relative error is less than 7.4% below 2 km, and reaches 22.8% at 5 km.

As an example for retrieval Δq, Fig. 3(a) shows the retrieval of molecular and AEC at 386 and 407 nm at 00:00 CST on March 2nd, 2014. In this case, AEC decrease with height below 5 km, and are roughly at the same level with molecular extinction coefficients above 5 km. The corresponding differential transmission ratio is illustrated in Fig. 3(b). The differences caused by Δq are less than 3.4% below 2 km, and reach as large as 8.7% at 10 km.

B. Cloud and the Boundary Layer Height Identification

The vertical structure of the atmosphere can be estimated by signals from AMPLE. Because of the relatively high backscatter coefficient inherent to aerosols and water droplets, aerosol layer or cloud can be detected by a continuous increase of the elastic backscatter lidar signal. There are several methods for determining the presence of aerosol layers and cloud, including the threshold method [29], the comparison with clear-sky [30] and the analysis of the signal derivative which is also known as the differential zero crossing method [31]. The threshold method is an effective tool to detect the step signals from noises [32], and is implemented to determine the base height of layers.

Moreover, it is necessary to distinguish between cloud and aerosol layers. In general, we use the slope of the signal to classify cloud, a method that has been developed by other researchers [33]. We calculate the logarithm gradient of RSCS as follows:

$$D(z) = \frac{d}{dz}\left(\mathrm{In}\left[P_\lambda(z)\, z^2\right]\right) \tag{4}$$

where $P_\lambda(z)$ is the elastic backscatter signal, and $P_\lambda(z)z^2$ refers to RSCS. The transitions between different layers can be characterized by the local minima of $D(z)$.

For an aerosol layer or cloud above the PBL, the local maximum and local minimum of quantity $D(z)$ are represented by T and B, respectively. When $z \leq 3$ km, if $B < -7$ or $T > 4$, the layer is identified as cloud. When $z > 3$ km, the layer is identified as cloud if $B < -7$ or $T > 2$. For the other situations, the layer is considered as aerosols.

In addition, the boundary layer height can be identified by the logarithm gradient method [34], [35]. The height Z_0 at which $D(z)$ reaches the first minimum is usually considered as the boundary layer height.

C. Calibration Method

The calibration constant C_w is generally determined by coincident RS data. However, due to the absence of simultaneous RS data, we select a typical day (March 2nd, 2014) with stable meteorological conditions. During this day, the PBL height is 585 m as retrieved by elastic backscatter signal at 08:00 CST. We use the RS above the PBL to determine the calibration constant. Using the regression method by England *et al.* [36], the calibration constant can be obtained by comparing the Raman signal ratio (averaged over 30 min from 04:30 to 05:00 CST) to the WVMR profile from RS (launched at 08:00 CST) within a height from 585 m (PBL) to 2500 m. With the calibration constant, the lidar profile can be presented at 04:45 CST. The profiles are averaged over 30 min. We apply a vertical smoothing window of 80 m below 1 km and 320 m above 1 km, as shown in Fig. 4(a).

Moreover, with the calibration constant, the lidar profile can be presented at 01:00, 02:00, 03:00, 04:00, and 04:45 CST [see Fig. 4(b)]. These WVMR profiles show stable characteristics above 600 m. Moreover, the WVMR continuously increases

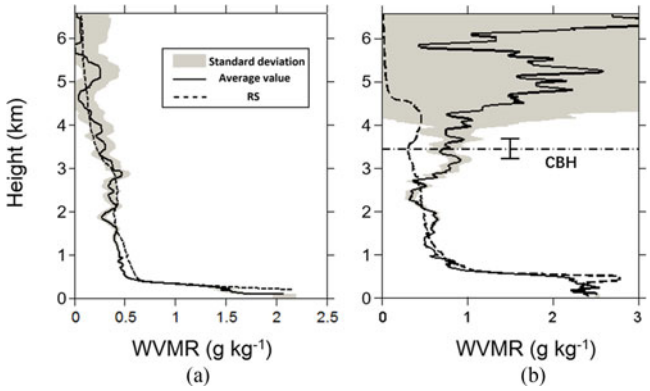

Fig. 5. WVMR profiles (black lines) from AMPLE averaged over 90 min (a) from 03:30 to 05:00 CST on March 7, 2014, and (b) from 03:30 to 05:00 CST on March 2, 2014. The dashed curves indicate the RS data which was launched at 07:15 CST at the same day. The gray areas indicate the standard deviation around the average value during this period. (a) and (b) Clear-sky and cloudy sky conditions, respectively. The mean CBH is marked as the horizontal dot dashed line in (b) and the error bar represents the variability of CBH during this time.

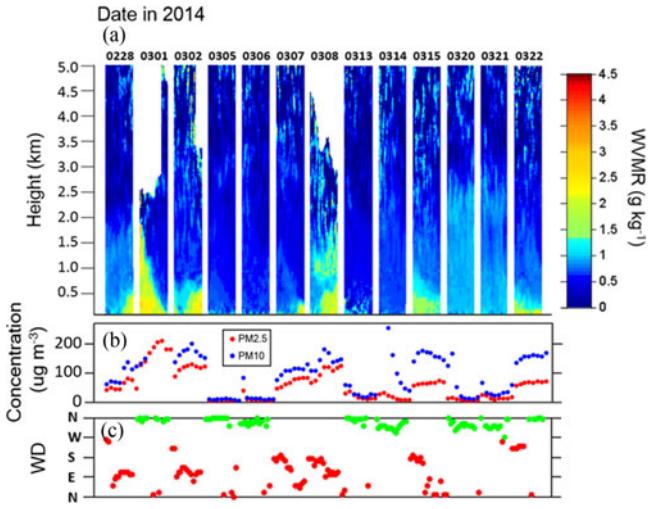

Fig. 6. (a) WVMR profiles measured by AMPLE for 13 nights. At each night, the WMVR measurement is from 22:00 to 05:00 CST. The region above cloud base has been removed. (b) Blue and red dots indicate simultaneous concentrations of $PM_{2.5}$ and PM_{10}, respectively. (c) Simultaneous WD. NW have marked as green dots; meanwhile, the winds came from other direction have marked as red dots.

near the surface. This phenomenon will be discussed in more detail in Section IV.

IV. Results

This section starts by discussing the cases of WVMR profile. In addition, WVMR retrievals for many nights are presented. With the observation of WVMR, the variation of water vapor associated with cloud and wind is discussed. The cloud base height (CBH) is determined by backscattering signals at 355 nm. The variation of relative humidity (RH) below clouds is demonstrated. The coupling between water vapor and aerosols is further examined with observation during a typical heavy pollution event.

A. Cases Study of Water Vapor Observation

We first compare the profiles of WVMR under cloudy and cloud-free conditions, in order to examine the impact of clouds on the vertical distribution of water vapor content.

The WVMR profiles are retrieved and averaged over 90 min starting at 03:30 CST on both March 7th [see Fig. 5(a)], and March 2nd, 2014 [see Fig. 5(b)]. Vertical smoothing window is 80 m below 1 km, increasing to 320 m between 1 and 3 km, and is 640 m above 3 km. For comparison, the WVMR profiles from RS launched at 08:00 CST on the same day are also shown. The profiles from AMPLE and RS agree well as indicated in Fig. 5(a). Clouds are observed from 03:30 to 05:00 CST. After 05:00 CST, clouds diminished. The averaged CBH is marked by the horizontal dot dashed line in Fig. 5(b), and the error bar represents the variability of CBH during the time period. Below 3 km, the profiles from AMPLE and RS (clear-sky) agree reasonably well. In the presence of cloud, the WVMR from AMPLE is comparatively higher than that from RS.

The standard deviation during the 90 min averaging window is plotted as the gray shades in Fig. 5. The amplitude of the standard deviation involves both the statistical fluctuation of the signal and changes in the water vapor content. As the Raman backscatter signals will be strongly interfered by clouds, the standard deviation dramatically increases above CBH, above which the retrievals of water vapor bear large uncertainties.

Because water vapor was retrieved over a sustained period of time, next we investigate the temporal evolution of WVMR during the entire measurement period. The change of water vapor with time for the 13 nights is demonstrated in Fig. 6(a). During each night, the WMVR measurement is made from 22:00 to 05:00 CST of the next day (e.g., in Fig. 6, 0228, the measurement is made from 22:00 CST on February 27th to 05:00 CST on February 28th). In Fig. 6(a), the temporal resolution is 30 min, and vertical smoothing window is 80 m below 1 km, and increases to 320 m above 1 km. Due to the disturbance of clouds to Raman signal which has been already shown in Fig. 5(b), the region above CBH has been removed in Fig. 6(a) based on clouds detected by the elastic backscatter signal. The WVMR is generally lower than 3 g·kg^{-1} during the observation time period, corresponding to the dry weather in Beijing in the spring. Simultaneous temporal evolutions of $PM_{2.5}$ and PM_{10} are presented in Fig. 6(b). The variability of $PM_{2.5}$'s concentration is found to agree well with that of water vapor content. High concentrations of water vapor and $PM_{2.5}$ together produce a favorable condition for the hygroscopic growth of aerosols and haze formation.

Moreover, we notice that the water vapor content is highly variable across different nights, and this phenomenon is found to be related with WD. For closer examination, concurrent WD condition is marked on Fig. 6(c). The northwesterly winds (NW) came from the arid and semiarid regions in northwest China and Mongolia, which is usually dry and cold. It is seen that March 1th, 5th, 6th, 13th, 14th, 20th, and 21th are dominated by persistent NW. The water vapor content is also significantly lower on March 1, and the WVMR level remains relatively

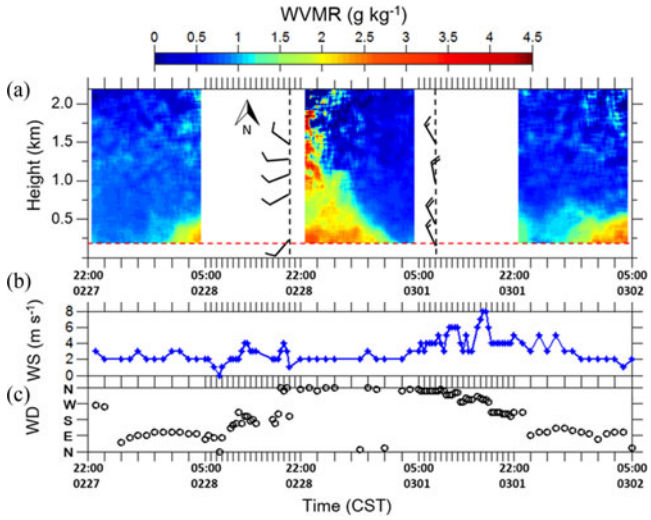

Fig. 7. (a) Temporal changes of WVMR vertical profiles taken between 22:00 CST on February 27th and 05:00 CST on 2 March 2014. (b) Simultaneous WS and (c) WD. The gaps in (a) represent period with missing data. In (a), (b), and (c), the time axis is compressed at daytime, with each scale representing 1 h. In (a), the wind profile from RS is labeled as station model.

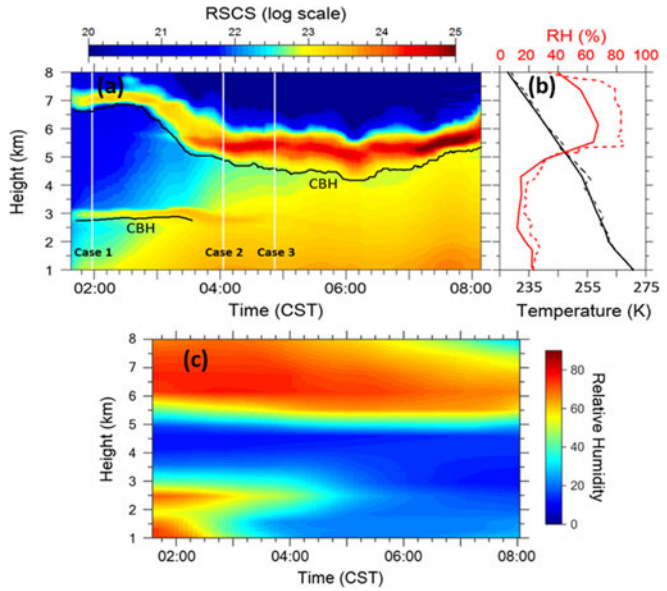

Fig. 8. (a) Temporal changes of the RSCS vertical profiles (log scale, arbitrary unit). The black line characterizes the CBH. (b) Temperature (dashed curve in black) and RH (dashed curve in red) profiles from RS which was launched at 07:15 CST on 1 March 2014. The solid curves in black and red indicate the temperature and RH profiles from modeling at 07:30 CST on 1 March, respectively.

low on March 5th, 6th, 13th, 14th, 20th, and 21th. Consistent with WVMR, the concentration $PM_{2.5}$ is also relatively low on March 5th, 6th, 13th, 14th, 20th, and 21th corresponding to NW. This coherency between water vapor and $PM_{2.5}$ suggests that WD might be the major factor contributing to the low moisture and pollution levels during this period, as well as pollution. To be mentioned, the concentration PM_{10} does not share the same evolution trend with WVMR. This is particularly evident for March 14th, when the concentration of PM_{10} is quite high, while water vapor and $PM_{2.5}$ levels stay low. This phenomenon is likely caused by the transport of large dust particles from the northwest arid region, which is a major component of PM_{10} but not $PM_{2.5}$.

To further clarify the impact of wind on water vapor, the evolution of water vapor during three consecutive nights is presented in Fig. 7(a). The three nights are from 22:00 CST February 27th to 05:00 CST March 2nd, and are hereafter named as "first night," "second night," and "third night" for convenience. The corresponding WS and WD are shown in parallel in Fig. 7(b) and (c), respectively.

With respect to the WD, wind mainly came from the East during the first and the third night, while its direction shifted to northwest at the second night. Meanwhile, the variation of WVMR also displays different characteristics during different nights. An increasing tendency in WVMR variability is observed for the first and the third night, whereas for the second night, WVMR exhibits a decreasing trend. This contrast is reasonable as the NW originated from inland, and is dry and cold, thus effectively reducing water vapor concentration. On the other hand, the East wind came from the seaward, which is warmer and contains more moisture and causes an increase in water vapor.

As shown in Fig. 7(a), the wind profiles from RS are labeled as station model at 20:00 CST on March 1st and at 08:00 CST on March 2nd. Between these two times, the wind field experienced a rapid change, with WS increased from 5–6 to 7–10 $m \cdot s^{-1}$, and WD switched from southwest to northwest. Coherent with wind data, the WVMR shows an evident uniform decrease at the second night.

The variation of WVMR at these three consecutive nights clearly demonstrates the impact of WS and WD on water vapor evolution. High water vapor content is usually associated with winds blowing from seaward, while strong NW will result in an abrupt reduction of WVMR.

B. *Evolution of Water Vapor Below Cloud*

In this section, we focus on the variability of water vapor below clouds. Fig. 8(a) shows examples of RSCS at 355 nm under cloudy condition from 01:40 to 08:10 CST on March 1st, 2014. The signals are averaged over a 16 min interval, and the vertical smoothing range is 80 m. Due to enhanced backscattering of large cloud droplets, the elastic backscatter signal starts to increase dramatically at cloud base. As a conventional way, the threshold method can effectively retrieve the CBH. Two cloud layers have been observed from lidar signals, and the base of the cloud layers is marked as the black line in Fig. 8(a). AMPLE cannot penetrate clouds with large optical thickness. Obviously, the signals are attenuated above 7 km from 04:00 CST to 08:00 CST.

Because no collocated meteorology observations are available on site, we use the weather research forecasting (WRF) model [37] to simulate the time series of temperature and humidity profiles on March 1st, 2014. This case used NCEP FNL (Final) Operational Global Analysis data as the initial field, and performed a 24-h forecast in two nested domains, with the

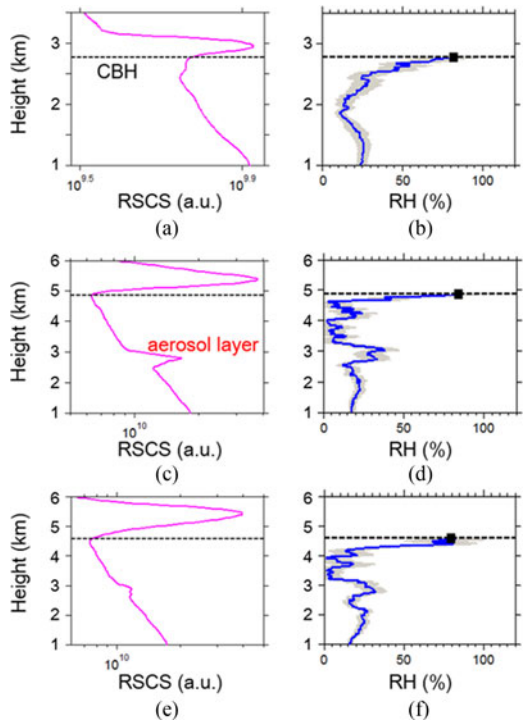

Fig. 9. Lidar observed RSCS and RH profiles showed in (a) and (b) on 01:58 CST (case 1), (c) and (d) 04:03 CST (case 2), and (e) and (f) 04:52 CST (case 3). The black dash lines indicate CBH.

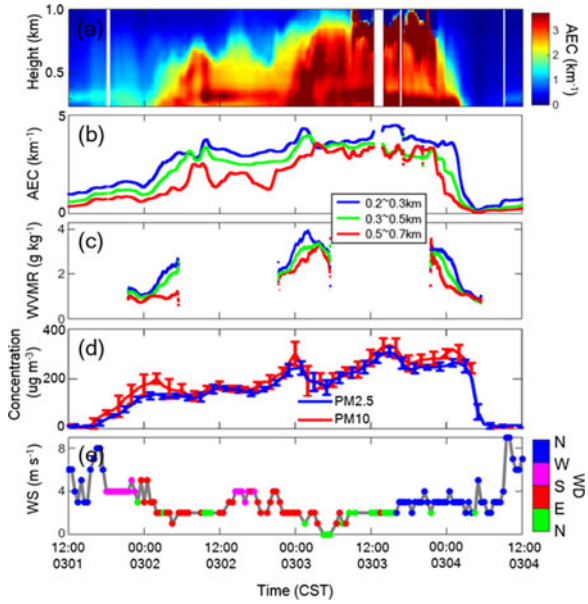

Fig. 10. (a) Time series of AEC vertical profiles taken between 12:00 CST on March 1st and 12:00 CST on March 4th 2014. In (b) and (c), blue, green, and red lines indicate the temporal changes of averaged AEC (b) and WVMR (c) at height ranges of 0.2–0.3, 0.3–0.5, and 0.5–0.7 km, respectively. (d) Blue and red lines indicate the temporal changes of concentrations of $PM_{2.5}$ and PM_{10}, respectively. The concentrations represent the mean value derived from nine environmental monitoring stations (see Fig. 1), and error bar indicate its standard deviation. (e) Simultaneous WS and WD. The northwest, southwest, southeast, and northeast winds are marked as blue, pink, red, and green dots, respectively.

horizontal resolution of 18 and 6 km, respectively. The observation site is located at the center of domain 2. The time step of the model was set to be 60 s, and the model outputs profiles at the location of observation site with a 5-min interval. In Fig. 8(b), the dashed curves in black and red represent temperature and RH profiles, respectively, from the RS launched at 07:15 CST on March 1st. The RS has been elevated to 5 km altitude along with the balloon at about 07:30. The temperature (solid curve in black) and RH (solid curve in red) profiles from modeling at 07:30 CST on March 1st are also shown. The temperature profiles agree well between WRF modeling and RS. The RH profiles from modeling and RS both significantly increase above 5 km, which is likely associated with the presence of the cloud layer. A cloud layer is observed around 5 km during the period as indicated by Fig. 8(a). In addition, Fig. 8(c) shows the RH profiles from modeling between 01:40 to 08:10 CST. There are two peaks in RH profiles around 2–3 and 6–8 km, which may again be associated with clouds that are independently observed by AMPLE.

As WRF model shows solid ability to estimate temperature profiles [38], we use the vertical profile of temperature derived from the WRF model to estimate the RH for a period in our observation of WVMR from 02:00 to 08:00 CST on March 1st. The RSCS and RH profiles for cases 1, 2, and 3 (marked in Fig. 8) are presented in Fig. 9. The RH profile is averaged over 16 min, with a vertical smoothing of 420 m. In Fig. 9(b), (d), and (f), the standard deviation of RH profiles during the averaging time (16 min) is marked by gray shading. The CBH is marked as the black dashed line and squares in Fig. 9. Because the Raman signals are disturbed beyond the cloud base, the RH profile is neglected above CBH. In Fig. 9(b), (d), and (f), RH is found to have a sudden increase just below the cloud. In particular, RH has increased by about 50% within 500 m from the cloud base. Moreover, RH stays mostly above 80% at cloud base.

Note that in case 2, there is an increase in RSCS at around 2.5 km [see Fig. 9(c)]. According to the classification criteria described in Section III, this layer is classified as aerosol layer. Relatively high RH is also found within this layer [see Fig. 9(d)]; high RH may be the important reason of formation of this aerosol layer due to hygroscopic growth effect of aerosols. Compared to case 1, the slope of RSCS in this layer is lower than that for cloud and its RH is much lower than 100%.

C. *Application to a Haze Episode*

We further examined a typical haze episode from 12:00 CST March 1st to 1200 CST March 4th using our lidar system. Fig. 10(a) represents the evolution of AMPLE retrieved AEC profiles during this period. We can clearly see a heavy pollution process starting around 00:00 CST March 2nd all the way up to 00:00 CST March 4th, with a sharp dissipation process after 00:00 March 4th. The AEC level maintains high throughout March 3rd. For better identification of aerosol vertical structure, we plot the time series of AEC at height ranges of 0.2–0.3, 0.3–0.5, and 0.5–0.7 km [see Fig. 10(b)]. In general, AEC decreases with height. However, during the period with the heaviest pollution (the whole day of March 3rd), AEC is high throughout the mixed layer which reaches ~0.9 km. Nighttime WMVR

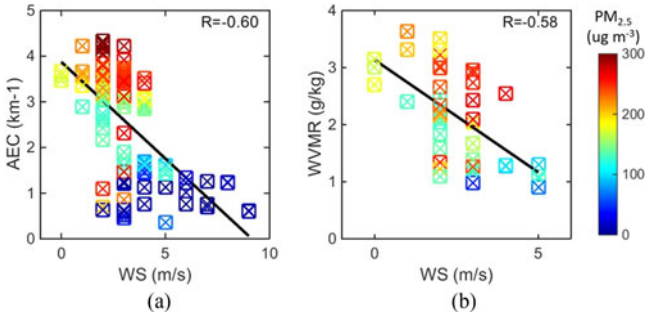

Fig. 11. (a) Correlation between AEC at height range of 0.2–0.3 km and WS. (b) Correlation between WVMR at height range of 0.2–0.3 km and WS. The black line illustrates the linear regression, and *R* represent the correlation coefficient. The color of the square indicates the corresponding concentration of $PM_{2.5}$.

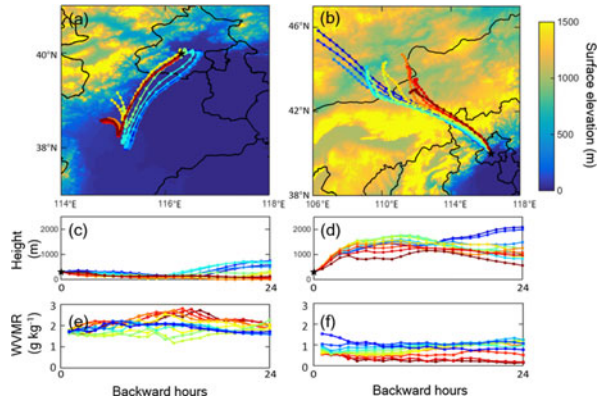

Fig. 12. One-day backward trajectories of air masses computed with the HYSPLIT model for (a) 00:00 CST to 12:00 CST March 2nd, and (b) 01:00 CST to 13:00 CST March 4th, 2014. Each line represents backward trajectories arriving along the cruise track at 300 m above sea level. The black stars indicate the lidar site. In (c) and (d), each line presents the corresponding evolution of air mass's elevation above sea level along with air mass's movement. In (e) and (f), each line presents the corresponding evolution of WVMR of air mass along with air mass's movement.

for the same period is also shown at different height ranges in Fig. 10(c), which indicate similar evolution trends as aerosols, partly due to the hygroscopic growth of aerosols [39]. AEC within the mixed layer also agrees well with PM_{10} and $PM_{2.5}$ concentrations, with the highest correlation found at 0.2–0.3 km altitude range [see Fig. 10(d)]. Fig. 10(e) represents the coincident wind condition. NW dominates before and after the haze process, corresponding to low aerosol concentration, whereas during the haze process, WD switched to south and WS stayed low. The relationship between AEC/$PM_{2.5}$ concentrations and WS can be better identified in Fig. 11, which clearly indicates that high AEC and $PM_{2.5}$ conditions are associated with low WS and vice versa. WVMR also exhibit a similar correlation with WS as aerosols.

For better understanding the accumulation and dispersion processes of the haze, backward trajectories of air masses in the lower atmosphere were calculated using NOAA's hybrid single-particle Lagrangian trajectory (HYSPLIT) model [40], [41]. One-day backward trajectories of air masses are computed by the HYSPLIT model, ending from 00:00 CST to 12:00 CST March 2nd and from 01:00 CST to 13:00 CST March 4th 2014, which correspond to the accumulation and dispersion period of haze respectively (see Fig. 12). For the accumulation process of haze, the air masses came from the southern part of the North China Plain with low altitude and high WVMR content [see Fig. 12(a) and (c)]. Because Beijing is surrounded by mountains in the north which serve as a natural barrier for air mass dispersion, water vapor and aerosols transported from the south will build up in the Beijing area. The high content of water vapor and aerosols forms an ideal environment for haze formation. In the dispersion process of haze, air masses came from the northwest arid area, which is usually cold and dry [see Fig. 12(b) and (d)]. These dry air masses serve as an effective cleaning mechanism of water vapor and aerosols, and push the humid, polluted air masses further southward.

The haze formation process is further studied in detail, the WVMR and AEC measurement from 22:00 CST on March 1st to 05:00 CST on March 2nd is presented [see Fig. 13(a) and (b)]. We especially focus on the evolution of water vapor and pollution at different altitudes. By comparing the time series of AEC and WVMR concentration at different altitudes, we find

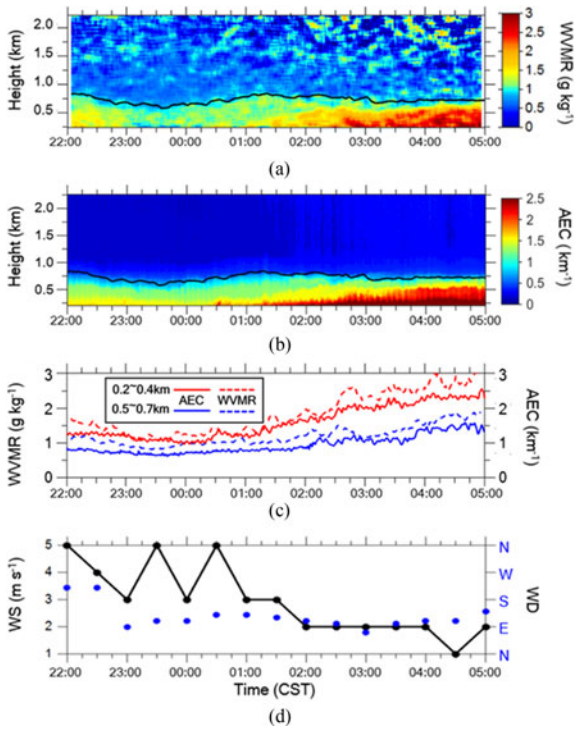

Fig. 13. (a) Temporal changes of WVMR vertical profiles and (b) AEC vertical profiles taken between 22:00 CST on March 1st and 05:00 CST on March 2nd 2014. (c) Solid red and blue lines indicate the temporal changes of average WVMR at height ranges of 0.2–0.5 and 0.5–0.7 km, respectively, while the dashed red and blue lines indicate the temporal changes of averaged AEC at these two height ranges. (d) Simultaneous WS and WD. In (a) and (b), the black lines indicate the PBL top.

that the lower altitude (0.2–0.4 km) has both higher AEC and WVMR concentration and variability [see Fig. 13(c)]. Moreover, there is also a timing difference in the haze accumulation process. For the 0.2–0.4 km range, AEC and WVMR began to increase after 00:00 CST on March 2nd, while for 0.5–0.7 km, they did not increase until 02:00 CST.

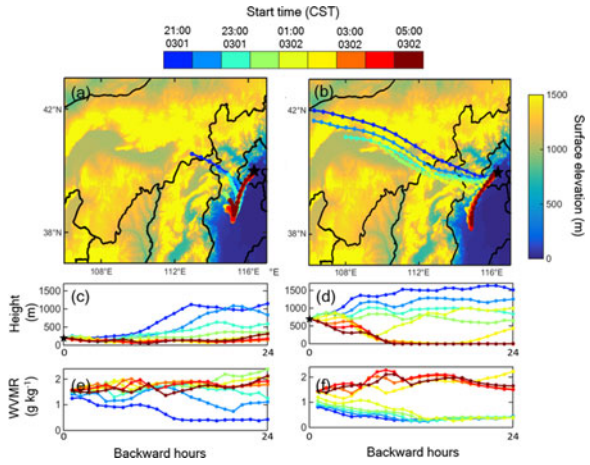

Fig. 14. One-day backward trajectories of air masses computed with the HYSPLIT model for 21:00 CST March 1st to 05:00 CST March 2nd, 2014. Each line represents backward trajectories arriving along the cruise track at (a) 200 m and (b) 700 m above sea level. The black stars indicate the lidar site. In (c) and (d), each line presents the corresponding evolution of air mass's elevation above sea level along with air mass's movement. In (e) and (f), each line presents the corresponding evolution of WVMR of air mass along with air mass's movement. The color of each line presents the end time of backward trajectory.

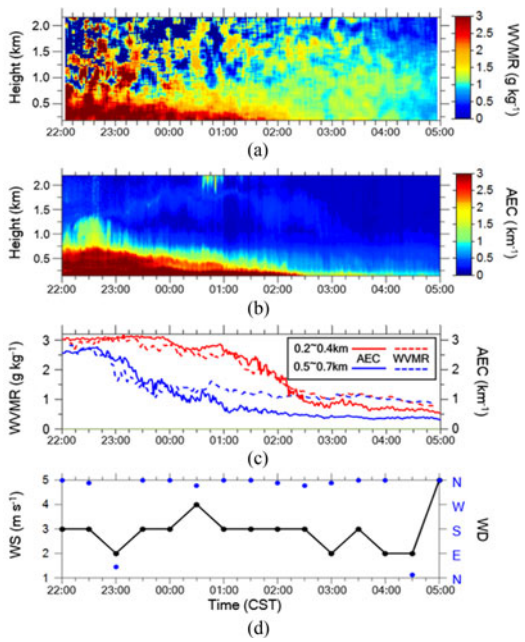

Fig. 15. (a) Temporal changes of WVMR vertical profiles and (b) AEC vertical profiles taken between 22:00 CST on March 3rd and 05:00 CST on March 4th 2014. (c) Solid red and blue lines indicate the temporal changes of average WVMR at height ranges of 0.2–0.4 and 0.5–0.7 km, respectively, while the dashed red and blue lines indicate the temporal changes of averaged AEC at these two height ranges. (d) Simultaneous WS.

The delayed increase of water vapor and aerosols for higher altitudes is further studied using the HYSPIT model, the results of which are presented in Fig. 14. One-day backward trajectories ending at 21:00 CST March 1st to 05:00 CST March 2nd 2014 for two heights 0.2 km [see Fig. 14(a)] and 0.7 km [see Fig. 14(b)] are calculated and different colors represent different ending times (see Fig. 14). We can see that air masses at 0.2 km

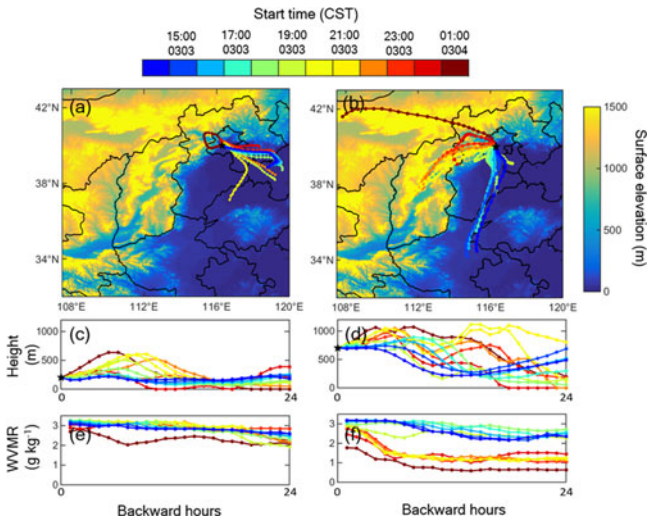

Fig. 16. One-day backward trajectories of air masses computed with the HYSPLIT model for 14:00 CST March 3rd to 01:00 CST March 4th 2014. Each line represents backward trajectories arriving along the cruise track at (a) 200 m and (b) 700 m above sea level. The black stars indicate the lidar site. In (c) and (d), each line presents the corresponding evolution of air mass's elevation above sea level along with air mass's movement. In (e) and (f), each line presents the corresponding evolution of WVMR of air mass along with air mass's movement. The color of each line presents the end time of backward trajectory.

generally come from the south and the WVMR remained high after 00:00 CST March 2nd, whereas the air masses at 0.7 km came from the northwest before 02:00 CST March 2nd but shifted to the south with higher water vapor content after 02:00 CST March 2nd. The different origins of air masses for different height likely explain the delayed increase of AEC and WVMR for higher altitude.

In the haze dispersion process, pollutant and water vapor at different altitudes also exhibit different characteristics. Fig. 15 shows the time series of AEC and WVMR at the two height ranges as well as that for WS. Different for the accumulation process, we notice that AEC and WVMR at higher altitudes decrease earlier [see Fig. 15(c)]. Again we examine HYSPLIT back trajectories for these two heights [see Fig. 16]. At 0.2 km, air masses mostly come from the sea with higher water vapor content, helping to maintain the high WVMR level. At 0.7 km, air masses also come from seaward first but switched to the west around 22:00 CST on March 3rd, reducing WVMR level. The haze decay process at different altitudes is again well explained by the different air mass sources.

V. Conclusion and Discussion

In this study, we presented Raman lidar retrieval of water vapor during the spring dry season in Beijing. To our knowledge, this is the first time that such high-resolution measurement of water vapor is made in the North China Plain. The AMPLE lidar system is able to reliably measure WVMR in the lower and middle troposphere. The information retrieved is sufficient to reveal atmospheric processes (e.g., cloud formation, wind variation, and weather change). The high-resolution products reveal more details about atmosphere and offers new opportunities

for the study of clouds and the boundary layer. We also investigated the variability of WVMR associated with wind, clouds, and aerosols. This study is helpful for understanding the causes of water vapor variability and its interaction with meteorology/aerosols in the Beijing area, and also has implications for many other regimes, especially other mega cities in the world.

Clouds have critical influences on the vertical distribution of water vapor. Water vapor shows high variability in the appearance of cloud. RH changes dramatically with cloud. As the standard deviation of WVMR measurements significantly increases above cloud base, the disturbance caused by cloud has been removed during the observational time period. Aerosol layers are also associated with relatively high water vapor content, and water vapor shows similar vertical structures and variation trend with aerosols. Moreover, water vapor evolution trend is heavily impacted by the wind field. We examined the variation of WVMR under different WS and WD conditions. The NW is the major factor for the reduction of moisture content. Besides, the WS also affects water vapor variability, and is negatively correlated with WVMR.

The causes of severe haze episodes in Beijing are complex and remain uncertain [42], [43], and our application of the AMPLE system provides useful insights into this research topic. The variability of water vapor and aerosols is found to be highly correlated. On one hand, the hygroscopic growth of some aerosol species which increases their extinction efficiency heavily depends on water vapor content. On the other hand, the accumulation and dispersion of water vapor and aerosols are both influenced by the WS and direction. Wind condition again exerts a major impact on the formation and dispersion of haze. In the PBL, there exhibits a delayed increase and an earlier decrease of water vapor and pollutants at higher altitudes compared to surface. The associated mechanism is further clarified using HYSPLIT back trajectory analysis.

The case study presented in this paper well demonstrates the usefulness of the Raman lidar technique in studying the temporal and vertical evolution of atmospheric water vapor. Our work delivers the message that the advanced Raman lidar system is quite suitable in studying the atmospheric processes associated with water vapor and aerosols, which should thus be of interest to the broad remote sensing community. In the future, we plan to apply our observation technique for a more comprehensive study of water vapor, clouds, wind, and aerosol optical properties for different seasons and geographic locations, in order to fully understand the nature of their interaction in the atmosphere.

ACKNOWLEDGMENT

The authors would like to thank the anonymous reviewers and the editors for their help in improving the manuscript.

REFERENCES

[1] S. Twomey, "Aerosols, clouds and radiation," *Atmos. Environ. Part A, Gen. Topics*, vol. 25, pp. 2435–2442, 1991.

[2] S. Melfi, J. Lawrence, and M. McCormick, "Observation of Raman scattering by water vapor in the atmosphere," *Appl. Phys. Lett.*, vol. 15, pp. 295–297, 1969.

[3] K. P. Shine and A. Sinha, "Sensitivity of the Earth's climate to height-dependent changes in the water vapour mixing ratio," *Nature*, vol. 354, pp. 382–384, Dec. 1991.

[4] A. M. Tompkins, "A prognostic parameterization for the subgrid-scale variability of water vapor and clouds in large-scale models and its use to diagnose cloud cover," *J. Atmos. Sci.*, vol. 59, pp. 1917–1942, Jun. 2002.

[5] J. P. Guo *et al.*, "Spatio-temporal variation trends of satellite-based aerosol optical depth in China during 1980-2008," *Atmos. Environ.*, vol. 45, pp. 6802–6811, Dec. 2011.

[6] Z. H. Rao, Z. M. Chen, H. Liang, L. B. Huang, and D. Huang, "Carbonyl compounds over urban Beijing: Concentrations on haze and non-haze days and effects on radical chemistry," *Atmos. Environ.*, vol. 124, pp. 207–216, Jan. 2016.

[7] R. A. Ferrare, S. H. Melfi, D. N. Whiteman, K. D. Evans, F. J. Schmidlin, and D. O. Starr, "A comparison of water vapor measurements made by Raman lidar and radiosondes," *J. Atmos. Ocean. Technol.*, vol. 12, pp. 1177–1195, Dec. 1995.

[8] T. Islam, P. K. Srivastava, and G. P. Petropoulos, "Variational bayes and the principal component analysis coupled with Bayesian regulation backpropagation network to retrieve total precipitable water (TPW) from GCOM-W1/AMSR2," *IEEE J. Sel. Topics Appl. Earth Observ. Remote Sens.*, vol. 8, no. 10, pp. 4819–4824, Oct. 2015.

[9] S. Sahoo, X. Bosch-Lluis, S. C. Reising, and J. Vivekanandan, "Optimization of background information and layer thickness for improved accuracy of water-vapor profile retrieval from ground-based microwave radiometer measurements at K-band," *IEEE J. Sel. Topics Appl. Earth Observ. Remote Sens.*, vol. 8, no. 9, pp. 4284–4295, Sep. 2015.

[10] D. N. Whiteman, S. H. Melfi, and R. A. Ferrare, "Raman lidar system for the measurement of water vapor and aerosols in the Earth's atmosphere," *Appl. Opt.*, vol. 31, pp. 3068–3082, Jun. 1992.

[11] J. E. M. Goldsmith, F. H. Blair, S. E. Bisson, and D. D. Turner, "Turn-key Raman lidar for profiling atmospheric water vapor, clouds, and aerosols," *Appl. Opt.*, vol. 37, pp. 4979–4990, Jul. 1998.

[12] C. Kiemle, A. Schafler, M. Wirth, A. Fix, and S. Rahm, "Detection and analysis of water vapor transport by airborne lidars," *IEEE J. Sel. Topics. Appl. Earth Observ. Remote Sens.*, vol. 6, no. 3, pp. 1189–1193, Jun. 2013.

[13] M. Wang, X. Fang, S. X. Hu, H. L. Hu, T. Li, and X. K. Dou, "Variation characteristics of water vapor distribution during 2000-2008 over Hefei (31.9 degrees N, 117.2 degrees E) observed by L625 lidar," *Atmos. Res.*, vol. 164, pp. 1–8, Oct. 2015.

[14] M. Froidevaux *et al.*, "A Raman lidar to measure water vapor in the atmospheric boundary layer," *Adv. Water Resour.*, vol. 51, pp. 345–356, Jan. 2013.

[15] D. Dionisi *et al.*, "Water vapor observations up to the lower stratosphere through the Raman lidar during the Maïdo Lidar Calibration Campaign," *Atmos. Meas. Techn.*, vol. 8, pp. 1425–1445, 2015.

[16] A. Foth, H. Baars, P. Di Girolamo, and B. Pospichal, "Water vapour profiles from Raman lidar automatically calibrated by microwave radiometer data during HOPE," *Atmos. Chem. Phys.*, vol. 15, pp. 7753–7763, 2015.

[17] S. H. Wu, G. Y. Dai, X. Q. Song, B. Y. Liu, and L. P. Liu, "Observations of water vapor mixing ratio profile and flux in the Tibetan Plateau based on the lidar technique," *Atmos. Meas. Techn.*, vol. 9, pp. 1399–1413, 2016.

[18] J. D. Blando and B. J. Turpin, "Secondary organic aerosol formation in cloud and fog droplets: A literature evaluation of plausibility," *Atmos. Environ.*, vol. 34, pp. 1623–1632, 2000.

[19] I. Tobin, S. Bony, and R. Roca, "Observational evidence for relationships between the degree of aggregation of deep convection, water vapor, surface fluxes, and radiation," *J. Climate*, vol. 25, pp. 6885–6904, Oct. 2012.

[20] Y. Zhao *et al.*, "Implementation of high dynamic Raman lidar system for 3D map of particulate optical properties and their time evolution," *Int. J. Remote Sens.*, vol. 3, pp. 240–244, 2013.

[21] S. H. Melfi, "Remote measurements of the atmosphere using Raman scattering," *Appl. Opt.*, vol. 11, pp. 1605–1610, 1972.

[22] V. Sherlock, A. Hauchecorne, and J. Lenoble, "Methodology for the independent calibration of Raman backscatter water-vapor lidar systems," *Appl. Opt.*, vol. 38, pp. 5816–5837, Sep. 1999.

[23] T. Leblanc, I. S. McDermid, and T. D. Walsh, "Ground-based water vapor Raman lidar measurements up to the upper troposphere and lower stratosphere for long-term monitoring," *Atmos. Meas. Techn.*, vol. 5, pp. 17–36, 2012.

[24] A. Bucholtz, "Rayleigh-scattering calculations for the terrestrial atmosphere," *Appl. Opt.*, vol. 34, pp. 2765–2773, May 1995.

[25] J. D. Klett, "Lidar inversion with variable backscatter/extinction ratios," *Appl. Opt.*, vol. 24, pp. 1638–1643, 1985.

[26] T. Takamura, Y. Sasano, and T. Hayasaka, "Tropospheric aerosol optical properties derived from lidar, sun photometer, and optical particle counter measurements," *Appl. Opt.*, vol. 33, pp. 7132–7140, Oct. 1994.
[27] U. Wandinger and A. Ansmann, "Experimental determination of the lidar overlap profile with Raman lidar," *Appl. Opt.*, vol. 41, pp. 511–514, Jan 2002.
[28] D. N. Whiteman *et al.*, "Raman lidar measurements during the International H2O Project. Part I: Instrumentation and analysis techniques," *J. Atmos. Ocean. Technol.*, vol. 23, pp. 157–169, Feb. 2006.
[29] C. M. Platt *et al.*, "The experimental cloud lidar pilot study (ECLIPS) for cloud-radiation research," *Bull. Amer. Meteorol. Soc.*, vol. 75, pp. 1635–1654, Sep. 1994.
[30] E. E. Clothiaux, G. G. Mace, T. P. Ackerman, T. J. Kane, J. D. Spinhirne, and V. S. Scott, "An automated algorithm for detection of hydrometeor returns in micropulse lidar data," *J. Atmos. Ocean. Technol.*, vol. 15, pp. 1035–1042, Aug. 1998.
[31] S. R. Pal, W. Steinbrecht, and A. I. Carswell, "Automated method for lidar determination of cloud-base height and vertical extent," *Appl. Opt.*, vol. 31, pp. 1488–1494, Apr. 1992.
[32] Z. Wang and K. Sassen, "Cloud type and macrophysical property retrieval using multiple remote sensors," *J. Appl. Meteorol.*, vol. 40, pp. 1665–1682, 2001.
[33] C. F. Zhao, Y. Z. Wang, Q. Q. Wang, Z. Q. Li, Z. E. Wang, and D. Liu, "A new cloud and aerosol layer detection method based on micropulse lidar measurements," *J. Geophys. Res.*, vol. 119, pp. 6788–6802, Jun. 2014.
[34] C. Flamant, J. Pelon, P. H. Flamant, and P. Durand, "Lidar determination of the entrainment zone thickness at the top of the unstable marine atmospheric boundary layer," *Boundary-Layer Meteorol.*, vol. 83, pp. 247–284, May 1997.
[35] Q. S. He, J. T. Mao, J. Y. Chen, and Y. Y. Hu, "Observational and modeling studies of urban atmospheric boundary-layer height and its evolution mechanisms," *Atmos. Environ.*, vol. 40, pp. 1064–1077, Feb. 2006.
[36] M. N. England, R. A. Ferrare, S. H. Melfi, D. N. Whiteman, and T. A. Clark, "Atmospheric water vapor measurements' comparison of microwave radiometry and lidar," *J. Geophys. Res.*, vol. 97, pp. 899–916, Jan. 1992.
[37] W. C. Skamarock and J. B. Klemp, "A time-split nonhydrostatic atmospheric model for weather research and forecasting applications," *J. Comput. Phys.*, vol. 227, pp. 3465–3485, Mar. 2008.
[38] A. Raju, A. Parekh, P. Sreenivas, J. S. Chowdary, and C. Gnanaseelan, "Estimation of improvement in Indian summer monsoon circulation by assimilation of satellite retrieved temperature profiles in WRF model," *IEEE J. Sel. Topics Appl. Earth Observ. Remote Sens.*, vol. 8, no. 4, pp. 1591–1600, Apr. 2015.
[39] E. Weingartner, H. Burtscher, and U. Baltensperger, "Hygroscopic properties of carbon and diesel soot particles," *Atmos. Environ.*, vol. 31, pp. 2311–2327, Aug. 1997.
[40] R. Draxler and G. Rolph, *HYSPLIT (HYbrid Single-Particle Lagrangian Integrated Trajectory) Model*. Silver Spring, MD, USA: NOAA Air Resour. Lab., 2003, [Online]. http://www.arl.noaa.gov/ready/hysplit4.html
[41] G. Rolph, *Real-Time Environmental Applications and Display sYstem (READY)*. Silver Spring, MD, USA: NOAA Air Resour. Lab., 2003 [Online]. http://www.arl.noaa.gov/ready/hysplit4.html
[42] S. Guo *et al.*, "Elucidating severe urban haze formation in China," *Proc. Nat. Acad. Sci. USA*, vol. 111, pp. 17373–17378, Dec. 2014.
[43] G. Wang *et al.*, "Persistent sulfate formation from London fog to Chinese haze," *Proc. Nat. Acad. Sci. USA*, vol. 113, pp. 13630–13635, 2016.
[44] J. Guo *et al.*, "The climatology of planetary boundary layer height in China derived from radiosonde and reanalysis data," *Atmos. Chem. Phys.*, vol. 16, pp. 13309–13319, 2016.

Tianning Su received the B.Sc. degree in atmospheric physics from Peking University, Beijing, China, in 2016, and is currently working toward the Ph.D. degree in atmospheric sciences at the University of Maryland, College Park, MD, USA.

His research interests include remote sensing techniques of lidar and the interaction between aerosols and clouds.

Jian Li received the B.Sc. degree in atmospheric physics from Peking University, Beijing, China, in 2012, where he is currently working toward the Ph.D. degree.

His research experience includes the average mixing ratio of CO_2 retrieved by a sun high resolution spectrometer and aerosols optical and physical properties over Beijing by a multiwavelength Raman Lidar.

Jing Li received the B.S. degree in atmospheric sciences from Peking University, Beijing, China, in 2006, and the Ph.D. degree in earth and environmental sciences from Columbia University, New York, NY, USA, in 2011.

From 2011 to 2015, she did research on atmospheric radiation and aerosol remote sensing at the NASA Goddard Institute for Space Studies. In 2015, she joined the Department of Atmospheric and Oceanic Sciences, Peking University, as an Assistant Professor, and continued to work on radiation and aerosol related research topics. Her current interest includes aerosol remote sensing and radiative effects, and the interaction between air pollution and meteorology.

Chengcai Li received the B.Sc., M.Sc., and Ph.D. degrees from Peking University (PKU), Beijing, China, in 1991, 1998, and 2002, respectively, all in atmospheric physics.

In 1991, he joined Heilongjiang Meteorological Bureau, China Meteorological Administration, when he graduated from PKU. From 1998 to 1999, he was a Research Assistant with the State Key Laboratory for Severe Storm Research, PKU. From 2001 to 2002, he was a Research Assistant with the Center for Coastal and Atmospheric Research, The Hong Kong University of Science of Technology, Clear Water Bay, Hong Kong, where he was a Postdoctoral Research Associate from 2002 to 2004. In 2004, he joined the Department of Atmospheric Sciences, School of Physics, PKU, as an Assistant Professor and is currently an Associate Professor. His research experience includes satellite and light detection and ranging remote sensing of clouds and aerosols, GPS remote sensing of precipitable water, application of remote sensing products on air pollution study, and aerosol physical and optical *in situ* measurements. His teaching includes undergraduate and graduate courses on atmospheric radiation and atmospheric remote sensing.

Yiqi Chu received the B.Sc. degree in atmospheric physics from Peking University, Beijing, China, in 2013, where he is currently working toward the Ph.D. degree in atmospheric physics.

His research interests include short-term prediction of meteorological elements in boundary layer and the inversion of ground-based microwave radiometers.

Yiming Zhao was born in Taiyuan, China, in 1983. She received the B.S. degree in electrical science and technology from Shanxi University, Taiyuan, in 2004, and the Ph.D. degree in physical electronics from Beijing University of Aeronautics and Astronautics, Beijing, China, in 2009.

She is currently a Senior Engineer at Beijing Research Institute of Telemetry, Beijing. Her main research interests are in the field of application of laser technology, include development of lidar, atmospheric and ocean environmental monitoring.

Jianping Guo received the Ph.D. degree in cartography and geographical information systems from the Institute of Remote Sensing Applications, Chinese Academy of Sciences, Beijing, China, in 2007.

From 2007 to 2009, he was with the Chinese Academy of Meteorological Sciences, Beijing, where he was an Assistant Professor of aerosol remote sensing. From 2009 to 2014, he was an Associate Professor with the same institute. Since 2014, he has been a Professor and one of the leading Principle Investigator for a state key project entitled "Haze/Fog Observational Studies" funded by the Ministry of Science and Technology of China. His current research interests include aerosol remote sensing and aerosol–cloud–precipitation interaction from both observation and modeling

Yong Yu was born in Changchun, China, in 1971. He received the B.S. degree in electric machinery from Harbin University of Science and Technology, Harbin, China, in 1993, and the M.S. degree in vibration shock noise and the Ph.D. degree in aircraft design from Harbin Institute of Technology, Harbin, in 1998 and 2001, respectively.

He joined Beijing Research Institute of Telemetry, Beijing, in 2001, and began work on synthetic aperture radar (SAR). He is currently a Research Fellow at BRIT. His current research interests include the application and development of SAR and lidar remote sensing.

Lidong Wang was born in Xinzhou, China, in 1987. He received the B.S. degree in optical information science and technology from Yanshan University, Qinhuangdao, China, in 2009, and the M.S. degree in optical engineering from Beijing Institute of Technology, Beijing, China, in 2012.

He is currently an Engineer at Beijing Research Institute of Telemetry, Beijing. His main research interests are in the field of lidar remote sensing and data processing and analysis.